

# Sensitivity of Southern California Wind Energy to Turbine Characteristics

Scott B. Capps<sup>1</sup>, Alex Hall<sup>1</sup> and Mimi Hughes<sup>2</sup>

<sup>1</sup>Department of Atmospheric and Oceanic Sciences, University of California, Los Angeles, CA 90095

<sup>2</sup>Cooperative Institute for Research in Environmental Sciences, University of Colorado, and NOAA/Earth System Research Laboratory, Boulder, CO

## ABSTRACT

Using output from a high-resolution meteorological simulation, we evaluate the sensitivity of southern California wind energy generation to variations in key characteristics of current wind turbines. These characteristics include hub height, rotor diameter, and rated power, and depend on turbine make and model. They shape the turbine's power curve and thus have large implications for the energy generation capacity of wind farms. For each characteristic, we find complex and substantial geographical variations in the sensitivity of energy generation. However, the sensitivity associated with each characteristic can be predicted by a single corresponding climate statistic, greatly simplifying understanding of the relationship between climate and turbine optimization for energy production. In the case of the sensitivity to rotor diameter, the change in energy output per unit change in rotor diameter at any location is directly proportional to the weighted average wind speed between the cut-in speed and the rated speed. The sensitivity to rated power variations is likewise captured by the percent of the wind speed distribution between the turbines rated and cut-out speeds. Finally, the sensitivity to hub height is proportional to lower atmospheric wind shear. Using a wind turbine component cost model, we also evaluate energy output increase per dollar investment in each turbine characteristic. We find that rotor diameter increases typically provide a much larger wind energy boost per dollar invested, though there are some zones where investment in the other two characteristics is competitive. Our study underscores the need for joint analysis of regional climate, turbine engineering, and economic modeling to optimize wind energy production. Copyright © 2011 John Wiley & Sons, Ltd.

## KEYWORDS

Wind Energy, Wind Turbine Characteristics, Atmospheric Science

**Correspondence**

E-mail: scapps@atmos.ucla.edu

DOI: 10.1002/we

Received ...

**1. INTRODUCTION**

Annual U.S. wind power capacity additions peaked in 2009, followed by a decrease in 2010 due to the economic downturn [1]. Growth in annual capacity relative to 2010 occurred in 2011 [2] with an upward trend expected to continue into the near future [3]. Overall, wind project performance, after experiencing a steady increase since 2005, leveled off in 2009 and 2010, resulting from lower wind resources, wind power curtailment and slowed growth in turbine hub height and rotor diameter [1]. A rebound in performance during 2011 is thought to be attributed to better wind resources across the U.S. [2]. Improvements in low-wind speed technology in addition to hub height and rotor diameter increases are fueling continued growth in capacity factors for certain wind resource classes [4]. A key difficulty in maximizing wind farm performance is matching the energy extraction capabilities of turbines to the meteorological characteristics at the wind farm location (e.g., [5, 6, 7]). Wind turbine characteristics having the largest implications for the turbine's performance are rotor diameter, rated power and hub height [8]. The sensitivity of annual energy production (AEP) to changes in any of these three characteristics is highly dependent on the climatological wind speed distribution at the location of interest. One goal of our study is to understand this dependence, and develop simple principles to characterize it. Because of its complex topography, the southern California region allows for the exploration of a wide variety of wind distributions and corresponding AEP sensitivities. This allows us to perform our analysis in the context of a wide variety of wind speed distributions, greatly increasing the likelihood that our main conclusions can be extended to other regions. For wind speed distributions, we rely on a high-resolution, validated regional meteorological simulation.

Potentially complicating the optimization problem further is that turbine costs vary significantly from one make to another. Even if a certain turbine configuration is better suited for energy generation than another at a particular location, it may be so much more expensive to manufacture that it may not qualify as the optimal investment choice. We estimate the cost increment associated with each turbine characteristic change with the help of an existing turbine component cost model [9]. This wind turbine characteristic cost benefit analysis therefore integrates high-resolution wind speed data, turbine specifications and power curves, and a turbine component cost model. To our knowledge, such a joint analysis of

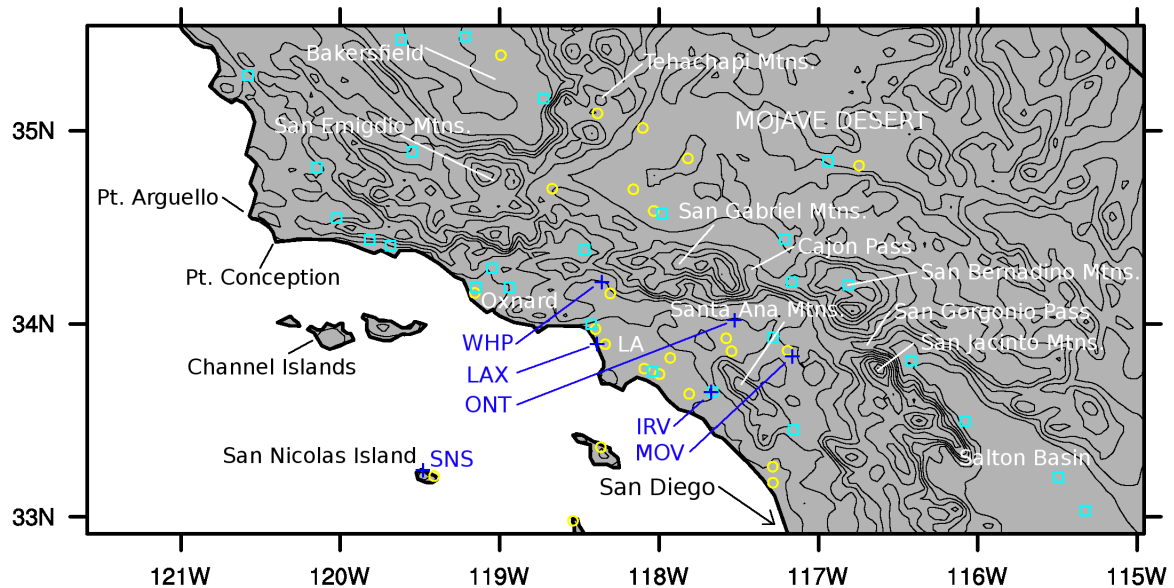


**Figure 1.** WRF simulation 3km resolution innermost domain with major geographic features and cities labeled. In this and all subsequent figures, the five gridcells along the domain boundaries have been removed. Dark blue crosses and labels mark the location of the profiler stations. The National Climatic Data Center (NCDC) and the California Irrigation Management Information System (CIMIS) surface observation station locations are marked with yellow circles and cyan squares, respectively.

regional climate, turbine engineering, and economic modeling to optimize wind energy production has not been performed before.

The study is presented as follows: The regional meteorological simulation is detailed in section 2.1, followed by a description of the turbine power curves used to estimate wind power for each turbine configuration in section 2.2. The meteorological simulation is then validated using near-surface and profiler observations in section 3. Next, we justify our determination of the ranges and incremental costs associated with the three primary wind turbine characteristics chosen for this study (Section 4). After presenting an overview of southern California wind energy (Section 5), AEP sensitivities to changes in rotor diameter, rated power and hub height are explored (Section 6). Finally, we present the estimates of the energy gains per dollar invested for each turbine component in section 7.

## 2. METEOROLOGICAL SIMULATION AND DATA PROCESSING

### 2.1. Southern California Meteorological Simulation

The simulation for this study was done with version 3.3 of the National Center for Atmospheric Research (NCAR) Weather Research and Forecasting Model (WRF-ARW) [10]. The WRF simulation is configured with the Mellor-Yamada-Nakanishi-Niino (MYNN,[11]) TKE-based boundary layer scheme in conjunction with the Kain-Fritsch cumulus

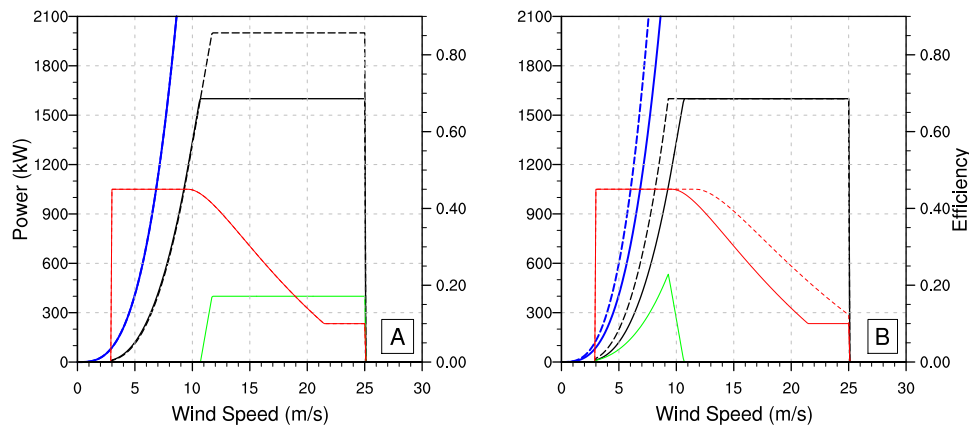


**Figure 2.** A baseline hypothetical wind turbine power curve consistent with current technology (cut-in speed= $3.0 \text{ m s}^{-1}$ , cut-out speed= $25.0 \text{ m s}^{-1}$ , rated power= $1.6 \text{ MW}$  and rotor diameter= $82.5 \text{ m}$ ) is plotted in both panels (solid black line). Changes to this baseline turbine include a change in rated power (from  $1.6$  to  $2.0 \text{ MW}$ , dashed lines in panel A) and rotor diameter (from  $82.5$  to  $100 \text{ m}$ , dashed lines in panel B). Also plotted, power difference at each wind speed (green lines), available wind power (blue) and turbine efficiency (red).

parameterization [12] (run in the 2 outer domains only). Radiation schemes selected within WRF include the Dudhia shortwave [13] from MM5 and the Rapid Radiative Transfer Model for longwave [14]. At the surface, the NOAH land surface model [15] is used along with the urban canopy model [16] with 3 urban development density categories. The three WRF nested domains have  $58 \times 51$ ,  $103 \times 85$  and  $214 \times 109$  gridpoints, corresponding to the 27, 9 and 3 km domains, respectively, each with 44 vertical levels. The highest resolution domain (Figure 1), spanning north-to-south from San Luis Obispo to San Diego and west-to-east from  $122^\circ \text{W}$  over the Pacific Ocean to just west of the Colorado River, resolves the main features of southern California's mountain ranges. The National Centers for Environmental Prediction's 3-hourly 32 km resolution North American Regional Reanalysis archive provides the necessary boundary conditions over the two year time period we analyze (Sept./2009–Aug./2011). WRF is initialized at 0000 UTC August 30 of each year (2009 and 2010) with analysis nudging applied to the outer domain to maintain model skill between initializations [17]. The first two days from each year are discarded as model spinup and all analysis in this study is derived from hourly outputs.

Within recent years, hub heights of installed wind turbines within the U.S. have averaged approximately 80 m with maximum heights of 100 m [2]. Thus, wind energy sensitivity to rotor diameter, rated power and hub height increments is explored for turbines with hub heights of 80, 100, and 120 m. The lowest 5 mid-level heights of our 44-level WRF simulation are 15, 57, 110, 165 and 219 m above the ground. Resolved winds at these heights are interpolated to 40, 60, 80, 100, 120, 140 and 160 m, providing 5 wind outputs across the rotor swept area for all hub heights and rotor radii examined here. To interpolate winds vertically, the heights of the 44 vertical  $\eta$  layers must be determined for each hour and all gridpoints. A cubic spline is then fit to the 8 lowest mid-layer resolved wind vector components, allowing for the

calculation of the interpolated wind vector components. Turbulence kinetic energy (TKE) and air density at each wind speed height, important for power curve corrections, are also extrapolated.

## 2.2. Wind Turbine Power Curves

Power curves are used to compute wind power for each hourly wind speed at each gridpoint (Power curve examples, which we discuss further below, are shown in figure 2). The power curve we choose as the baseline is derived from turbine characteristics predominantly found in U.S. installations (rated power of 1.6 MW, cut-in, rated and cut-out speed of 3.0, 10.7 and 25.0 m s<sup>-1</sup>, respectively) [1, 2]. We quantify the sensitivity of southern California wind energy to rated power, rotor diameter and hub height by imposing the effects of changes in these turbine characteristics on this baseline wind power curve. All 3-bladed horizontal axis wind turbine power curves created for this sensitivity study require some assumptions. First, discrete cut-in and cut-out speeds are assumed with no power generated for winds slower (faster) than the cut-in (cut-out) speed. Second, we assume the rotor extracts at most 45% of available wind power (see red lines in figure 2). This rotor efficiency is far below the Betz Limit (59.3% of available wind power is theoretically extractable according to this limit [18]) and near current technology specifications. Finally, power is constant for winds faster than the rated speed, with rotor/generator speed regulated by the control system (e.g., changing the blade pitch).

Power curves give average electrical power generated by a turbine as a function of hub height wind speed given standard atmospheric conditions with low turbulence intensities. However, air density variations stemming from fluctuations in temperature and pressure can also affect power. Thus, it is necessary to use the following formula to adjust power curve wind speeds for variations in air density:

$$U_{cor} = U_{act} * (\rho_{act}/\rho_{std})^{1/3} \quad (1)$$

where  $U_{act}$  and  $U_{cor}$  is the actual and corrected wind speed,  $\rho_{act}$  and  $\rho_{std}$  is actual and standard atmosphere air density (1.225 kg m<sup>-3</sup>), respectively. Previous studies have found an improved correlation between wind power and a wind speed averaged across the entire rotor swept area compared to a single hub height wind speed [19, 20]. Thus, wind power calculated in this study is a function of an equivalent wind speed ( $U_{eqv}$ ) consisting of a rotor-averaged wind speed, including turbulent energy effects ([21, 19]):

$$U_{eqv} = \frac{1}{A_r} \sum_{i=1}^n A_i \sqrt[3]{\bar{U}_i^3 (1 + 3I_i^2)} \quad (2)$$

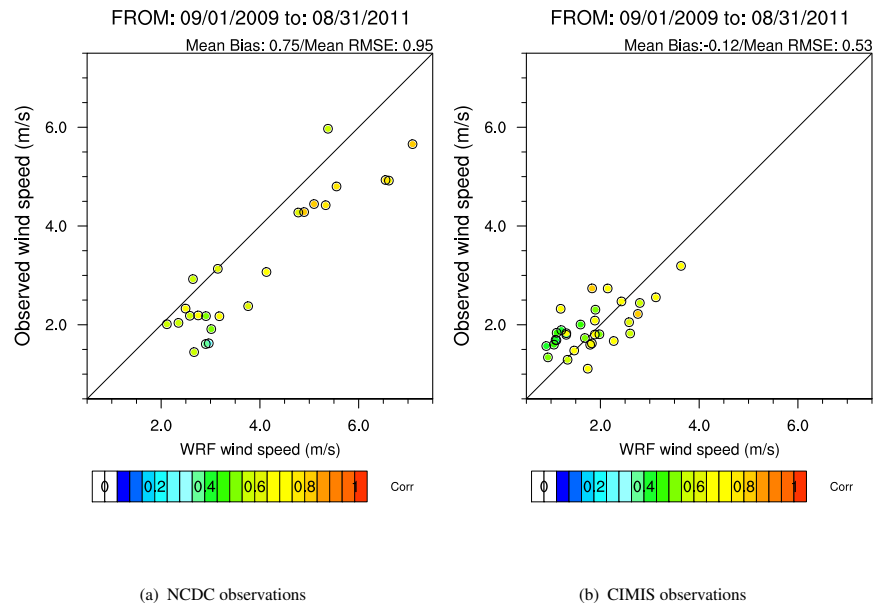


**Figure 3.** Scatter plot of near-surface daily average wind speeds for NCDC (Panel a) and CIMIS (Panel b) station observations and each closest WRF gridcell over the period Sept. 2009 through Aug. 2011. Colors show the Spearman rank correlation for daily average wind speeds between WRF and the nearest station observations. WRF’s daily average wind speed mean bias and RMSE is shown at the top.

where  $U_i$  is the wind speed at each height  $i$ ,  $A_r$  is the rotor swept area,  $A_i$  is the circular segment area intersected by the winds at each height and  $I$  is turbulence intensity calculated from WRF’s turbulence kinetic energy (TKE) assuming isotropic turbulence:

$$I = \frac{\sqrt{\frac{2}{3}TKE}}{\bar{U}} \tag{3}$$

At the WRF vertical resolution used in this study and for all hub heights examined, 5 wind speed levels intersect the rotor swept area for rotor diameters of 82.5 and 100 m, respectively. The isotropic turbulence assumption can introduce some error into the energy sensitivities calculated within this paper since turbulence is often anisotropic. Using 3-dimensional wind component standard deviations from 2010–2011 IRV SODAR measurements (see Figure 1 for location), we estimate the hourly average error in rated power, rotor diameter and hub height wind energy sensitivities calculated in this paper to range from  $-1.70\%$  to  $-0.70\%$ ,  $-3.63\%$  to  $-1.87\%$  and  $-3.48\%$  to  $-1.24\%$ , respectively. Also, equivalent wind speed does not consider directional wind shear across the rotor diameter which can lead to a high energy bias in areas prone to high, persistent directional wind shear.

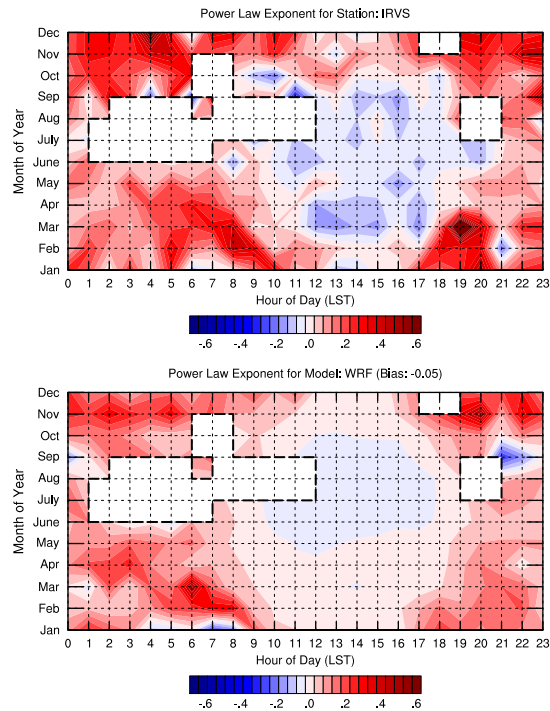


**Figure 4.** Climatology of hourly Irvine SODAR (top) and WRF (bottom) power law exponents between 80 and 120 m spanning Sept. 2010 to Sept. 2011. Winds slower than  $3 \text{ m s}^{-1}$  and faster than  $25 \text{ m s}^{-1}$  were removed. Location of IRVS SODAR station shown in figure 1.

### 3. OBSERVATIONAL COMPARISON

The main conclusions of this paper depend on WRF's ability to realistically simulate winds throughout the boundary layer across the region of interest. Near surface winds of the Pennsylvania State University-National Center for Atmospheric Research Mesoscale Model (MM5, WRF's predecessor) compared well against observations when run at higher (e.g., [22]) and lower resolution (6 km) for this region (e.g., [23, 24, 22, 25]). While a growing number of studies have validated WRF wind energy centric variables against observations for regions across the world (e.g., [26, 27, 28, 29, 30]), we know of no studies for the region of interest here. Furthermore, model performance is not only dependent upon resolution and configuration but is site specific as well. Therefore, we compare our WRF simulation against wind speed observations from 55 surface stations and a SODAR station. Near surface wind speeds were obtained from the National Climatic Data Center (NCDC, <http://www.ncdc.noaa.gov/oa/ncdc.html>) and the California Irrigation Management Information System (CIMIS, <http://www.cimis.water.ca.gov/cimis/>) at locations shown in figure 1. To facilitate a fair comparison, WRF's 10m winds were extrapolated to the station anemometer height using the log-law. CIMIS station anemometers are mounted at 2 m above the ground while anemometer heights of the NCDC stations are typically between 7 and 10 m. As a result, CIMIS station winds are typically slower than NCDC winds (Comparing figures 3(b) and 3(a)). Consistent with the WRF AEP

geographical distribution (figure 6), NCDC stations west of the coastal ranges have slower mean wind speeds compared to desert and offshore stations, forming two clusters in figure 3(a). When compared to NCDC stations, WRF has a fast wind speed bias (Mean bias of  $0.75 \text{ m s}^{-1}$ , figure 3(a)) and a slight negative bias compared to CIMIS stations (Mean bias of  $-0.12 \text{ m s}^{-1}$ , figure 3(b)). Average WRF RMSE for daily average wind speeds is  $0.95 \text{ m s}^{-1}$  and  $0.53 \text{ m s}^{-1}$  for NCDC and CIMIS observations, respectively. With the exception of two (five) NCDC (CIMIS) station locations, daily average WRF winds are well-correlated (Spearman rank correlations greater than 0.50) with observations across the region.

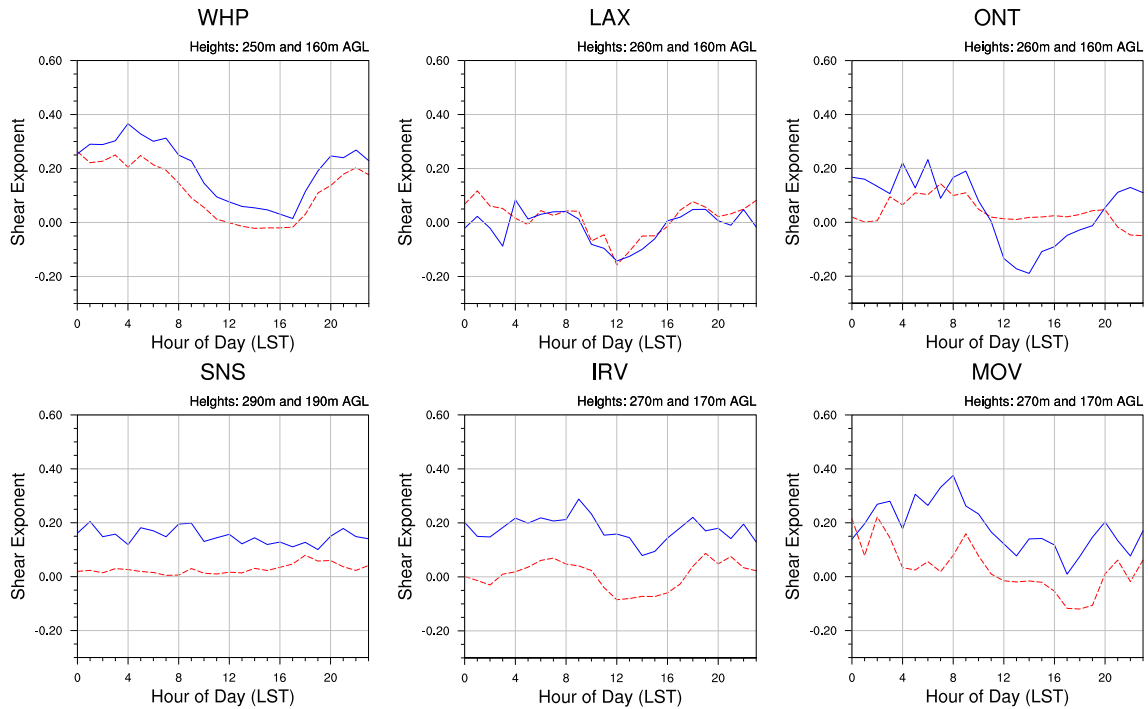


**Figure 5.** Sept. 2009 to Sept. 2011 WRF (red, dashed line) and profiler (blue, solid line) hourly wind shear exponent climatologies between heights denoted in upper right-hand corner of each plot at Whiteman Airport (WHP), Los Angeles Int'l Airport (LAX), Ontario (ONT), San Nicolas Island (SNS), Irvine (IRV) and Moreno Valley (MOV). Note: Heights differ depending upon the profiler station.

While WRF seems to capture horizontal variability in near-surface wind speed with reasonable accuracy, the conclusions of this study also rest partly on WRF's ability to represent the vertical wind profile near the surface. Although WRF's representation of the wind speed profile is an improvement over assuming a simple power law estimate with a constant  $\alpha = 1/7$ , WRF's wind profile may not be perfectly realistic (e.g., [26, 31, 29]). Furthermore, WRF's ability to accurately predict this profile is dependent upon the vertical resolution and configuration ([27]). Therefore, validation of our WRF configuration's wind profile is warranted. For the timespan and domain of our WRF configuration, we have one SODAR (IRV, measuring hourly winds starting at 30 m above the ground AGL to 200 m) and six radar boundary layer profilers

(BLPs) (which measure hourly winds above 140 m AGL) (see Figure 1 for locations). For both the SODAR and BLPs, we compare observations to the output of the highest correlated WRF gridpoint within 6 km.

The SODAR observations were provided by the South Coast Air Quality Management District every 15 minutes at 10 m vertical resolution. Erroneous SODAR measurements can occur resulting from external noise, rainfall, clouds and atmospheric stability. We attempt to limit erroneous SODAR winds by discarding measurements with vertical velocities greater than  $1 \text{ m s}^{-1}$ , possibly occurring during rain events ([32]). The remaining top of hour SODAR measurements were selected for a comparison against corresponding WRF instantaneous hourly output for winds between 3 and  $25 \text{ m s}^{-1}$ . There are inherent differences between WRF and SODAR winds which should be noted before this comparison. WRF winds are instantaneous and spatially-average over the gridcell extent while SODAR wind components are measured independently by observing a volume of air (on the order of tens of cubic meters) and vector-averaged over a 10-15 minute period ([32]). Figure 4 compares the WRF and observed wind shear exponent,  $\alpha$ , calculated between wind speed heights of 80 and 120 m from the power law expression:

$$U(z) = U_r \left( \frac{z}{z_r} \right)^\alpha \quad (4)$$

where  $U$  is the horizontal wind speed magnitude at height  $z$  (m) and  $U_r$  is the wind speed at the reference height  $z_r$  (80 m in this case). On average, WRF slightly underestimates vertical wind shear (bias=-0.02) compared to the SODAR measurements while following the diurnal cycle throughout the year fairly well. The well-mixed profile begins earliest during summer and extends past 7PM compared to 5PM during the winter. The WRF model and SODAR measurements both show high nocturnal  $\alpha$  values during fall and winter. However, WRF overestimates daytime wind shear between the months of October and March while underestimating daytime (between 10AM and 2PM) wind shear during the fall and winter months. Also, the sign of the power law exponent differs between WRF and the SODAR near 4am and 9pm during September, 10pm during March and 9-10am in October.

Quality controlled cooperative agency BLP data was obtained from the Meteorological Assimilation Data Ingest System (MADIS, <http://madis.noaa.gov/>). BLP's used in this study are operated by the South Coast Air Quality Management District and NOAA's Earth System Research Laboratory Physical Sciences Division. Both WRF and BLP winds were interpolated to AGL heights using linear interpolation. Although the heights of the BLP measurements are at or above the peak height of the rotor for our tallest wind turbine, it is possible that this comparison is indicative of WRF's skill across the turbine swept area. We required at least one BLP wind height to be within 40 m of the height of each interpolated wind

speed with at least one BLP wind speed at a height below the lowest interpolated wind height. Only wind speeds between 3 and  $25 \text{ m s}^{-1}$  were included. Figure 5 compares WRF and BLP hourly wind shear exponent climatologies at each BLP station location. WRF's wind shear exponent compares the best with the BLP at LAX throughout most of the day. For WHP, MOV and IRV, WRF's wind shear exponent is lower with respect to the BLP's for all hours but the diurnal cycle is replicated very well. For ONT, WRF's shear exponent diurnal cycle shows very little resemblance to the BLP's shear exponent. WRF systematically predicts a lower shear exponent at SNS, a site dominated by the marine boundary layer and thus characterized with a muted diurnal cycle.

## 4. WIND TURBINE CHARACTERISTIC RANGES AND COSTS

### 4.1. Hub Height

Three hub heights are selected to calculate the sensitivity of energy output to hub height. Hub height growth has slowed in recent years with 2010 and 2011 average U.S. installed turbine hub heights of 79.8 and 81 m, respectively [2]. Future innovations should allow for turbines with hub heights ranging from 80 up to 120 m. Thus, wind energy sensitivity to hub height is assessed using 80, 100 and 120 m hub heights (Results for 80 and 120 m shown). At each height, power is determined using the baseline power curve and equations 1 and 2, and the power outputs are compared.

### 4.2. Rated Power

The power gain associated with an increase in turbine rated power at every location in southern California is also quantified. This sensitivity is evaluated by increasing the baseline turbine's rated power while keeping all other characteristics identical (Figure 2, panel A). The two rated powers used (1.6 and 2.0 MW) straddle the 2011 average nameplate capacity (1.97 MW) of installed turbines within the U.S. [2]. The 1.6 MW (2.0 MW) wind turbine has a rated speed of  $10.7 \text{ m s}^{-1}$  ( $11.8 \text{ m s}^{-1}$ ). Thus, power differences between the two curves span wind speeds of  $10.7$  to  $25.0 \text{ m s}^{-1}$  (Figure 2, panel A, green line).

### 4.3. Rotor Diameter

Rotor diameters of turbines installed in the U.S. from 2009–2011 averaged 81.6, 84.3 and 89 m, respectively [2]. Wind energy sensitivity to rotor diameter is evaluated using rotor diameters of 82.5 and 100 m (Figure 2, panel B). With a larger rotor, the available power is larger (dashed blue curve) and the actual power extracted by the rotor is also larger (dashed

black line). More power is extracted for winds between the cut-in and rated speeds, leading to a somewhat slower rated speed. Power differences between the baseline power curve and the one associated with a larger rotor diameter rise steadily from the cut-in speed, peak at 290 kW near  $9.3 \text{ m s}^{-1}$ , and fall to 0 kW near  $10.7 \text{ m s}^{-1}$  (green lines in figure 2).

#### 4.4. Wind Turbine Characteristic Incremental Costs

The economic implications of the wind energy sensitivity to rated power, rotor diameter and hub height can only be assessed by estimating the incremental costs associated with the change in the turbine characteristics. Historically, determining a cost scaling model for wind turbine components has been a difficult task. Because of proprietary nondisclosures and rapid technological innovations in materials and design, pricing data has been sparse. However, after the mid-1990's, wind turbine configurations mainly converged to the 3-bladed, upwind horizontal axis design, making projects such as the U.S. Department of Energy's Wind Partnerships for Advanced Component Technology (WindPACT) studies possible. The "Wind Turbine Design Cost and Scaling Model" of Fingersh et al. [9] extends the WindPACT studies to achieve a cost model for modern turbine configurations. In this study, manufacturing and installation costs for three bladed, upwind pitch-controlled, variable-speed turbines with steel towers are scaled following Fingersh et al. [9] with the assumption that this cost model still accurately estimates incremental cost differences associated with the three turbine characteristics evaluated in this study. Fingersh et al. [9] provides cost equations that are typically functions of the component (e.g., tower, rotor, etc.) mass or turbine rated power. For example, rotor blade costs scale with blade mass which, depending upon materials, scales with rotor diameter. Cost and mass equations are provided for both baseline and advanced materials. Initial capital costs are inflated from 2002 to 2009 dollars using the Gross Domestic Product and the Producer Price Index for labor and materials, respectively.

Transportation costs vary depending upon the weight of the shipment, distance traveled and method of transportation (e.g., truck, train or barge). Fingersh et al. [9] provides transportation costs as a function of machine rating. However, because size and mass scales with all three of the characteristics evaluated here, transportation costs could scale with each characteristic change. Further, transportation distance will vary drastically depending on the supplier. For simplicity, we exclude incremental transportation costs associated with the three turbine characteristics. Additionally, we assume that offshore installation vessels have enough spare lifting capacity to accommodate a heavier turbine, so installation costs (already very high) would probably not increase.

To quantify incremental costs associated with hub height changes, we first determine which wind turbine components scale with hub height changes. The purpose of the tower (besides preventing rotor blades from hitting the ground) is to

raise the hub and rotor into faster, less turbulent winds aloft while withstanding aerodynamic and weight loads [33]. A larger rotor and taller tower result in a greater mass for the tower and supporting foundation. Thus, tubular steel tower and hollow drilled pier foundation costs scale with changes in hub height and rotor [9]. To calculate cost increments to hub height changes alone, we compute incremental tower and foundation costs while holding the rotor diameter constant (82.5 m). Based on tower heights of 80 and 100 m, our computed cost per meter increase in hub height, including assembly and installation, is \$6,680/m for a single turbine.

Following Fingersh et al. [9], component costs that scale with rated power changes include gearbox, mechanical brake, variable speed electronics, hydraulic and nacelle cover costs. Using the cost difference between an 2.0 and 1.6MW generator (assumed multi-path drive, permanent-magnet), estimated cost per kW increment in rated power is \$420/kW for a single turbine.

More turbine components scale with rotor diameter than with the two other characteristics explored in this study. Longer rotor blades must still be relatively lightweight while maintaining structural strength. Thus, increases in rotor diameter result in larger blade mass with higher labor and materials costs. Increased rotor blade mass and the aerodynamic loads of longer blades must be accompanied by a stronger hub and low-speed shaft, larger bearings, more powerful yaw drive and blade pitch mechanism, and a stronger mainframe, tower and foundation. Additionally, the nose cone and assembly/installation costs all scale with the rotor diameter. Our computed cost per meter rotor diameter increase is \$34,320/m for a single turbine (based on the cost difference between a 100 and 82.5 m rotor diameter, tower height of 80 m).

## 5. OVERVIEW OF SOUTHERN CALIFORNIA WIND ENERGY

In this section we provide a brief overview of the geographical distribution of simulated southern California AEP and its seasonality (Figure 6). Southern California AEP is first calculated using the baseline wind turbine power curve (Figure 2, solid black line, 80 m hub height). AEP varies by more than a factor of four across the region, from less than 2 GWh for the coastal plain and southern San Joaquin Valley to more than 8 GWh in the Tehachapi Mountains, San Gorgonio Pass and offshore near the Channel Islands (Figure 6, top panel). Wind energy patterns are clearly associated with terrain features in inland areas and match wind speed patterns reported elsewhere for this region ([34]). For example, in the Mojave Desert, AEP is approximately 6 GWh with energy increasing with elevation. Wind energy exhibits substantial seasonality over the entire southern California Bight (see Figure 6, bottom panel). The seasonal peak in wind energy occurs during spring

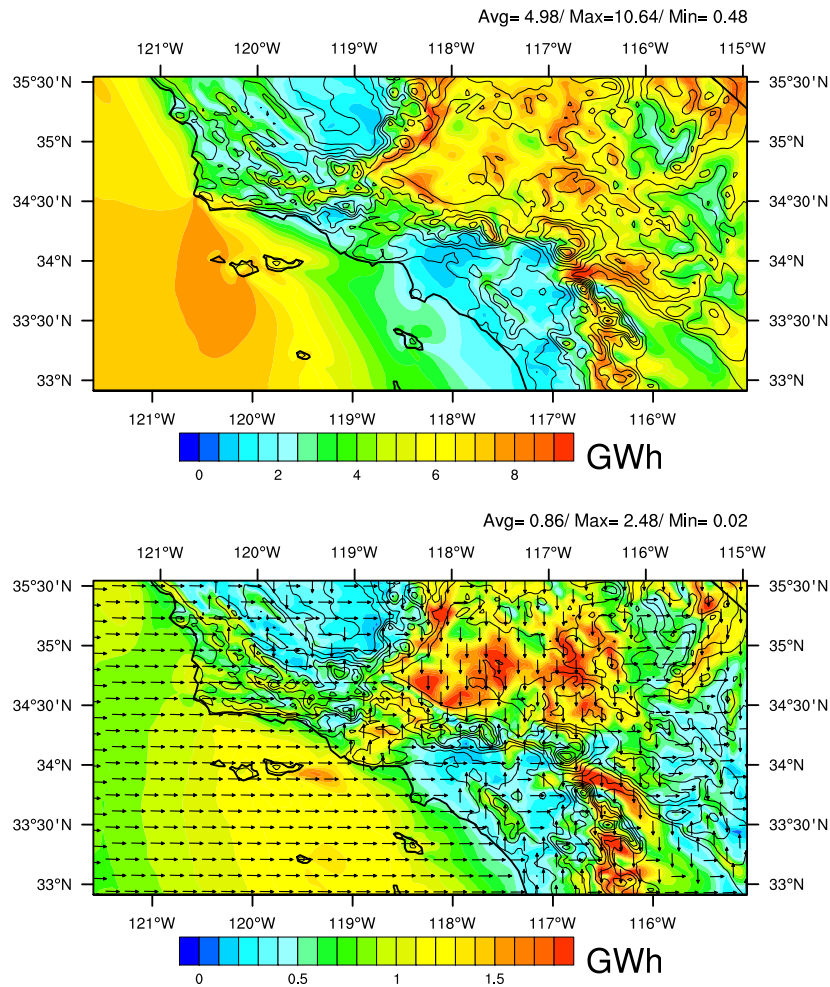


**Figure 6.** 2009–2011 annual energy production (AEP) for the baseline turbine with a hub height of 80 m (top panel). 2009–2011 range (maximum minus minimum) of seasonal wind energy (color shading) and season of peak wind energy (arrows, bottom panel: Up=DJF, Right=MAM, Down=JJA, Left=SON). Every third arrow shown for clarity.

for all offshore regions, when flow is typically from the northwest. In contrast, power dips during the winter months. For the majority of the southern California Bight, the amplitude of the energy seasonal cycle exceeds 0.9 GWh, a substantial fraction of the annual energy itself.

Wind energy also exhibits a complex pattern of seasonality over the southern California land areas, a reflection of the seasonality of the region's modes of atmospheric variability. Shoreward of the coastal ranges, wind energy peaks at most locations during winter, and at some locations, in spring. The predominance of the winter peak is likely due to the region's famous Santa Ana phenomenon. Santa Ana Winds occur approximately 2–5 days per month between September and April with peak frequency and intensity in the winter months [35, 23]. These strong offshore wind events result in peak wind power during December, January and February (DJF) on the shoreward side of the Tehachapi, San Gabriel,

San Bernadino, Santa Ana and Cuyamaca (San Diego County) mountains. Exceptions to this wintertime peak include the Los Angeles Basin and inland valleys not directly downstream of the mountain passes. Much slower winds during summertime in all these regions result in seasonal cycle amplitudes varying from less than 0.5 GWh for the coastal basins and valleys to more than 0.7 kW for the shoreward slopes. Higher seasonal amplitudes (more than 1 GWh) are found shoreward of the mountain gaps including the San Gorgonio and Cajon passes. The most expansive of these regions, with seasonal amplitudes of nearly 1.3 GWh, is found shoreward of the lower elevation zone between the San Gabriel and San Emigdio mountains. During a Santa Ana or northerly wind flow event, a strong jet often forms over this region, within and downwind of the wide mountain pass. During other flow regimes, especially those predominating in summertime, the region is relatively quiescent.

In contrast to the shoreward side, wind energy generally peaks during summer, and to a lesser degree, spring on the desert side of the coastal ranges and throughout the Mojave Desert. This is consistent with afternoon maximum onshore pressure gradients associated with the summertime heat low over the desert southwest. Most notable is the vast region in the Mojave Desert between the Tehachapis and the San Gabriels where strong summertime afternoon winds regularly funnel through the Tehachapi Mountains and collide with winds blowing over the lower elevations between the higher San Gabriel and San Emigdio mountains. The seasonal amplitudes of these regions (more than 1.6 GWh) are more than 18% of their AEP (more than 8.5 kW). The largest seasonal amplitude is found in the eastern portion of the San Gorgonio Pass. Containing many operating wind farms, this region has a seasonal amplitude of 2 GWh, more than 20% of its AEP (9 GWh).

## 6. SENSITIVITY OF WIND ENERGY TO TURBINE CHARACTERISTICS

### 6.1. Rotor Diameter

Figure 7 illustrates the sensitivities of AEP to rotor diameter changes and the origins of these sensitivities. AEP change per unit rotor diameter change (top panel) ranges from 25 MWh m<sup>-1</sup> for the coastal regions and inland valleys to greater than 80 MWh m<sup>-1</sup> along the spine of the Tehachapi Mountains, the lower elevations between the San Gabriel and San Emigdio mountains, Mojave Desert mountains and passes, the San Gorgonio Pass and the Laguna Mountains east of San Diego. Changes in rotor diameter affect power for wind speeds in the range of the power curve between the cut-in and rated speeds (See figure 2, panel B). For the hypothetical power curves used in this study, these are winds between 3 and 10.7 m s<sup>-1</sup>. Wind energy ought to be most sensitive to rotor diameter increments in regions where the bulk of the

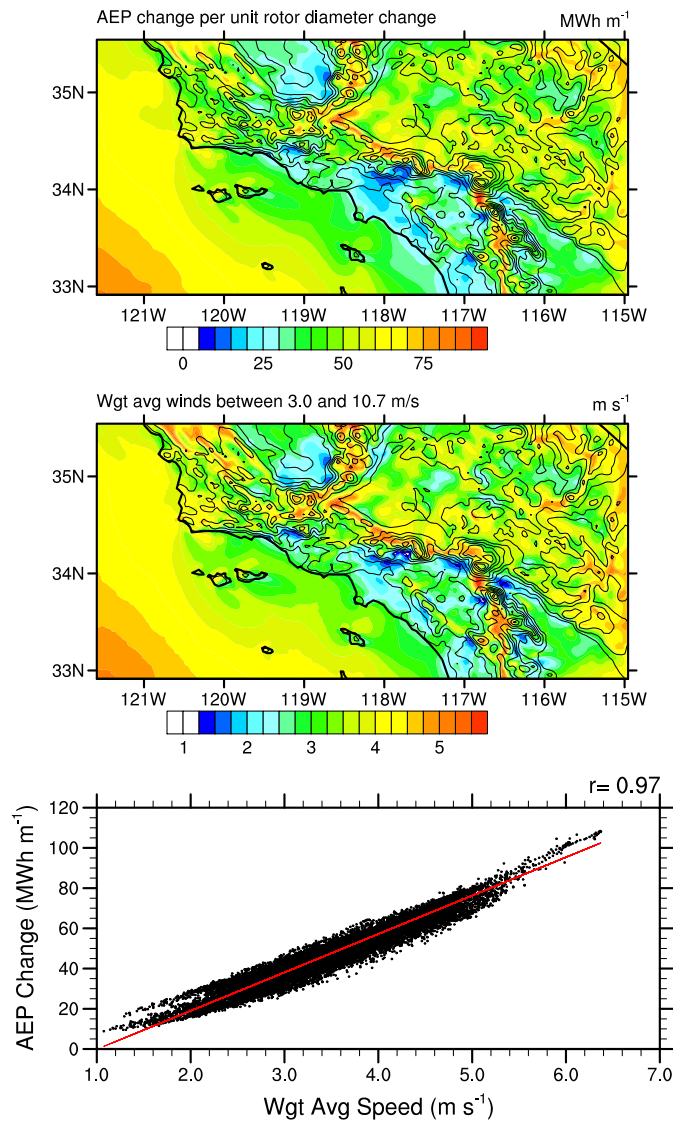


**Figure 7.** AEP change per unit rotor diameter change (top panel), weighted average between  $3\text{--}10.7 \text{ m s}^{-1}$  (middle panel) and scatter plot of the AEP change per unit rotor diameter change vs. weighted average wind speed between  $3\text{--}10.7 \text{ m s}^{-1}$  with regression line in red (bottom panel).

wind speed distribution is between the cut-in and rated speed. However, since wind power scales with the square of the rotor diameter between the cut-in and rated speeds, the power difference between two rotor diameters considered here varies non-linearly with wind speed (Figure 2, green line in panel B). To take into account this nonlinearity, we compare a weighted average wind speed between the cut-in and rated speed to the rotor diameter sensitivity. For the weighted average wind speed, wind speed bin frequencies are normalized by the sum of wind speed frequencies across the entire wind distribution

$$u_{w_{3-10.7}} = \frac{\sum_{i=1}^{n_1} u_i f_i}{\sum_{k=1}^{n_2} f_k} \quad (5)$$

where  $u_i$  is wind speed (weight averaged across the rotor swept area for an 80 m hub height and 82.5 m rotor diameter),  $f$  is the frequency,  $n_1$  is the wind speed count between the cut-in and rated speed and  $n_2$  is the wind speed count for all speeds. If this weighted average wind speed is high, then the larger difference between the two power curves at higher wind speeds should result in a higher sensitivity to rotor diameter changes.

Comparison of the top and middle panels confirms that this weighted average wind speed between the cut-in and rated speeds ( $u_{w,3-10.7}$ ) is an excellent predictor of rotor diameter sensitivity. In fact, rotor diameter sensitivity and weighted average wind speed have a nearly-linear relationship (correlation coefficient,  $r = 0.97$ ) (Figure 7, bottom panel). Thus, for every  $1 \text{ m s}^{-1}$  increase in weighted average wind speed, wind energy sensitivity to rotor diameter changes increases by approximately  $20 \text{ MWh m}^{-1}$ . The most sensitive regions (greater than  $80 \text{ MWh m}^{-1}$ ) listed above have weighted average speeds in excess of  $5 \text{ m s}^{-1}$ . Regions moderately sensitive to rotor diameter changes include offshore areas northwest of Point Arguello and west of San Nicolas Island, portions along the spine of the Tehachapi Mountains, the lower elevations between the San Gabriel and San Emigdio mountains, Mojave Desert and within the Laguna Mountains east of San Diego (Figure 7, top panel). These regions are all characterized with weighted average wind speeds of at least  $4 \text{ m s}^{-1}$ . In contrast, regions least sensitive to rotor diameter changes (less than  $40 \text{ MWh m}^{-1}$ ) include greater Los Angeles and San Diego, the Salton Basin and southern San Joaquin Valley. Finally, wind energy is most sensitive to rotor diameter increments ( $> 90 \text{ MWh m}^{-1}$ ) within the San Gorgonio pass collocated with the fastest weighted average wind speeds ( $> 5 \text{ m s}^{-1}$ ).

## 6.2. Rated Power

Changes in rated power affect power production for wind speeds between the rated speed (in this study,  $10.7 \text{ m s}^{-1}$ ) and the cut-out speed ( $25 \text{ m s}^{-1}$ ). In contrast to rotor diameter changes, wind power differences due to rated power changes are constant with wind speed, with the exception of the steep linear ramp near the rated speed (Figure 2, green line in panel A). Thus the AEP sensitivity to rated power changes at any given location ought to bear a close relationship to the proportion of the wind speed distribution between the rated and cut-out speed. The greater the fraction of time the wind speed is between the rated and the cut-out speeds, the greater the sensitivity to the turbine's rated power. Thus we expect a correspondence between the geographical patterns of the percent of the wind speed distribution between the rated and cut-out speed and the rated power sensitivity.

These geographical patterns are shown in the top and middle panels of figure 8. The extremely high spatial correlation between the two patterns ( $r = 0.99$ ) is quantified in the bottom panel of Figure 8. Regions surrounding the Channel Islands, along the desert slope of the Tehachapi Mountains, the mountains of the Mojave Desert and the San Gorgonio Pass

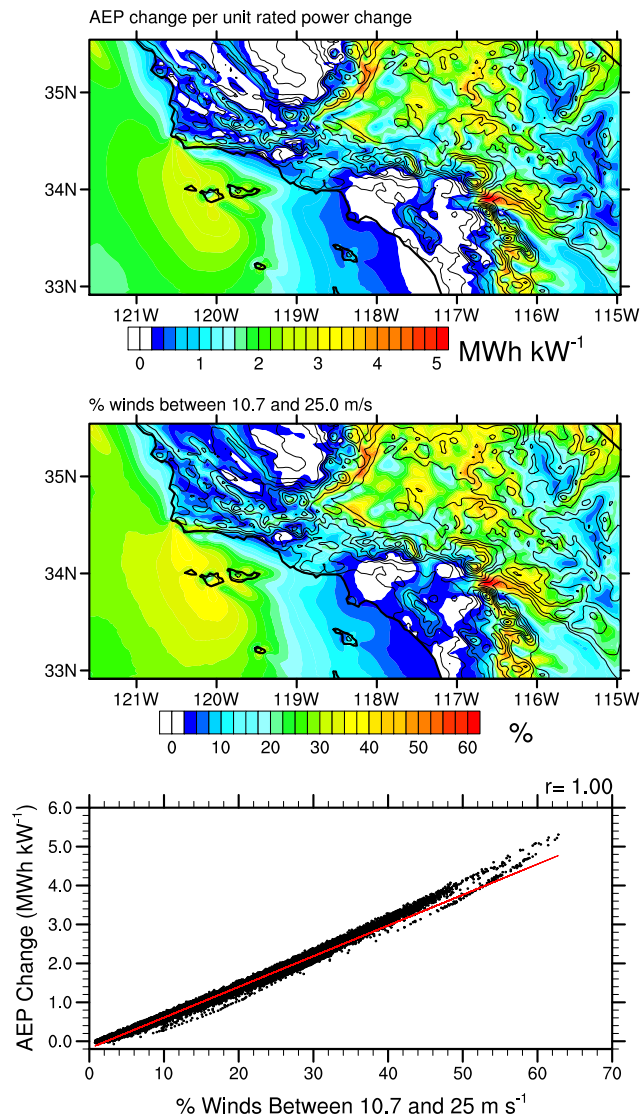


**Figure 8.** AEP change per unit rated power change (top panel). Percent of rotor swept area averaged wind speed distribution between  $10.7\text{--}25\text{ m s}^{-1}$  (middle panel). Scatter plot of the AEP change per unit rated power and the percent of distribution between  $10.7\text{--}25\text{ m s}^{-1}$  with regression line in red (bottom panel).

are the most sensitive to rated power increments (AEP change per unit rated power  $r$  changes exceeding  $3\text{ MWh kW}^{-1}$ ). These are regions where the upper-tail of the wind speed distribution reaches farthest past the rated speed. The high sensitivity to rated power in the Tehachapi and San Geronio passes arises from the fact that during summer, most of the wind speeds are between the rated and cut-out speeds. During winter, fast but relatively infrequent Santa Ana Winds boost wind speed frequencies between the rated and cut-out speed shoreward of the Cajon pass and the lower elevations between the San Gabriel and San Emigdio mountains. Hence, low-to-moderate AEP sensitivities to rated power increments ( $1 - 2\text{ MWh kW}^{-1}$ ) are seen in these regions. Regions near the Tehachapis, Mojave Desert mountains and the Channel Islands, while only moderately sensitive to rotor diameter changes, are more sensitive to rated power changes. More than

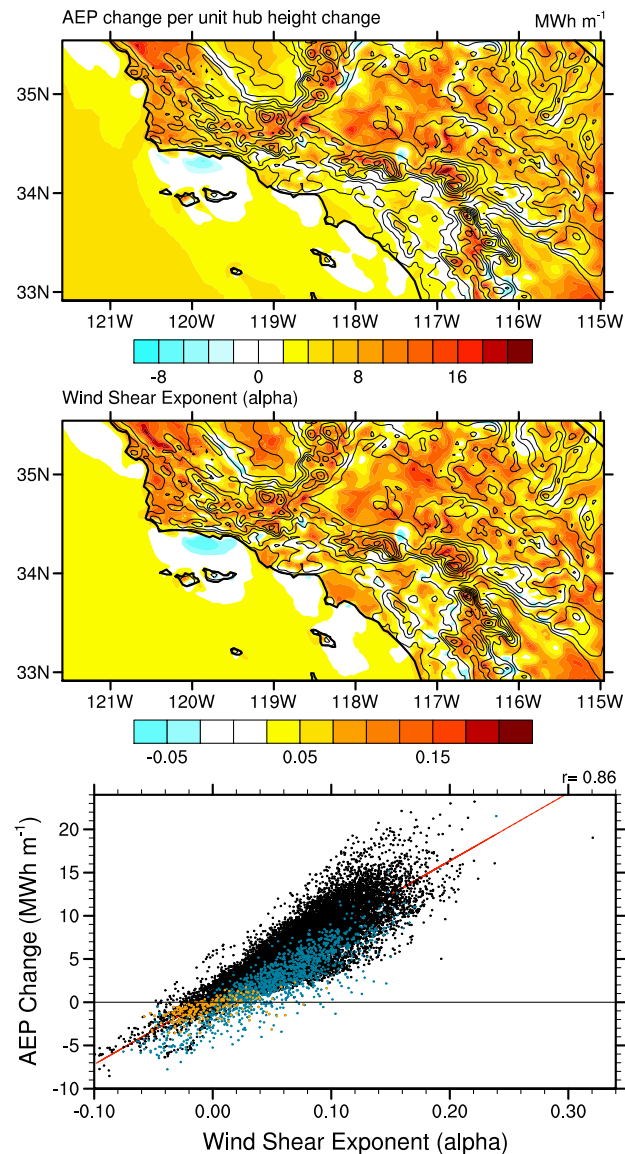


**Figure 9.** AEP change (120 m minus 80 m) per unit hub height increment for the baseline turbine (top panel) and average wind shear exponent for winds between 3 and 25  $\text{m s}^{-1}$  (middle panel). Scatter plot of AEP change per unit hub height increment and average wind shear exponent with regression line in red (bottom panel). Orange dots represent locations where the percent of the wind speed distribution between the rated and cut-out speed changed less than  $\pm 0.1\%$  from 80 m to 120 m. Blue dots indicate regions where the percent of the wind speed distribution exceeding the cut-out speed changed more than 0.20% from 80 m to 120 m.

half of the springtime distribution lies between the rated and cut-out speed for ocean waters between Point Conception and south and west of the Channel Islands (not shown). These fast winds are associated with the dominant northwesterly regime [23] of spring when the Pacific subtropical high strength and position is secure due the northward shift in the storm track. In contrast, less than 10% of the distribution reaches past the rated speed within the coastal regions of greater Los Angeles and San Diego, southern San Joaquin Valley and Salton Basin for all seasons, creating low sensitivity to rated power changes in these areas.

### 6.3. Hub Height

Figure 9 illustrates the sensitivity of AEP to hub height, and its origins. Most of the western Mojave Desert is relatively sensitive to hub height changes (greater than  $12 \text{ MWh m}^{-1}$ ) with moderate sensitivities in the eastern Mojave and Sonoran deserts (Figure 9, top panel). Furthermore, higher elevations more exposed to the free atmosphere are most sensitive to hub height changes. AEP is least sensitive to hub height changes (less than  $4 \text{ MWh m}^{-1}$ ) over portions of the coastal and inland basins and the coastal waters with the exception of the Oxnard Plain, Santa Clarita Valley and Santa Ana Mountains. Surprisingly, increasing the baseline wind turbine hub height results in equal or less average wind energy along the lower elevation slopes of most mountain ranges. This effect is most notable along the desert slopes of the Tehachapi Mountains.

The average vertical wind shear in the 80–120 m range may be a proxy for the change in energy output between the two levels if two conditions are met: (1) All wind speed anomalies have approximately the same characteristic vertical profile, and (2) the resulting characteristic wind speed distribution shift towards higher speeds is not confined to the range beyond the rated speed, where power generation is either insensitive to wind speed increases, or simply falls to zero beyond the cut-out speed. Vertical wind shear between 80 and 120 m is generally influenced by mean boundary layer wind speed and atmospheric stability. Thus, the vertical wind shear exponent ( $\alpha$ ) spatial pattern generally matches that of average wind speed (not shown), ranging from  $-0.05$  to  $0.20$  across southern California (Figure 9, middle panel). Over the inner coastal waters, mean winds are slower and vertical wind shear is less ( $0. \leq \alpha \leq 0.05$ ) compared to the outer waters ( $\alpha \approx 0.05$ ). Vertical wind shear is largest on land at higher elevations where there is a narrower vertical transition between the surface and the free atmosphere. For example, portions of the San Bernadino and San Jacinto mountains have the largest wind shear ( $\alpha$  exceeding  $0.2$ ). The lower elevations between the San Gabriel and San Emigdio mountains and Oxnard Plain also exhibit a large wind shear, which may be the signature of the fast Santa Ana Winds.

The relationship between wind energy sensitivity to hub height changes and vertical wind shear is evident when comparing the top and middle panels of figure 9. This correlation between vertical wind shear and wind energy sensitivity is confirmed in the bottom panel of figure 9 ( $r = 0.86$ ). This correlation, though very high, is less than perfect. The points straying below the regression line in figure 9 correspond to locations experiencing wind frequency shifts either (1) between the rated and cut-out speeds, where wind power is insensitive to wind speed increases, or (2) to beyond the cut-out speed, where wind power falls to zero in spite of the wind speed increase. For instance, the energy generated at 120 m could be less than at 80 m for very fast wind speed regions where 120 m winds exceed the cut-out speed more often than 80 m. Blue markers in the bottom panel of figure 9 denote locations where the wind speed distribution upper-tail expands the most beyond the cut-out speed going from hub heights of 80 m to 120 m. The power loss from increased cut-out events at most

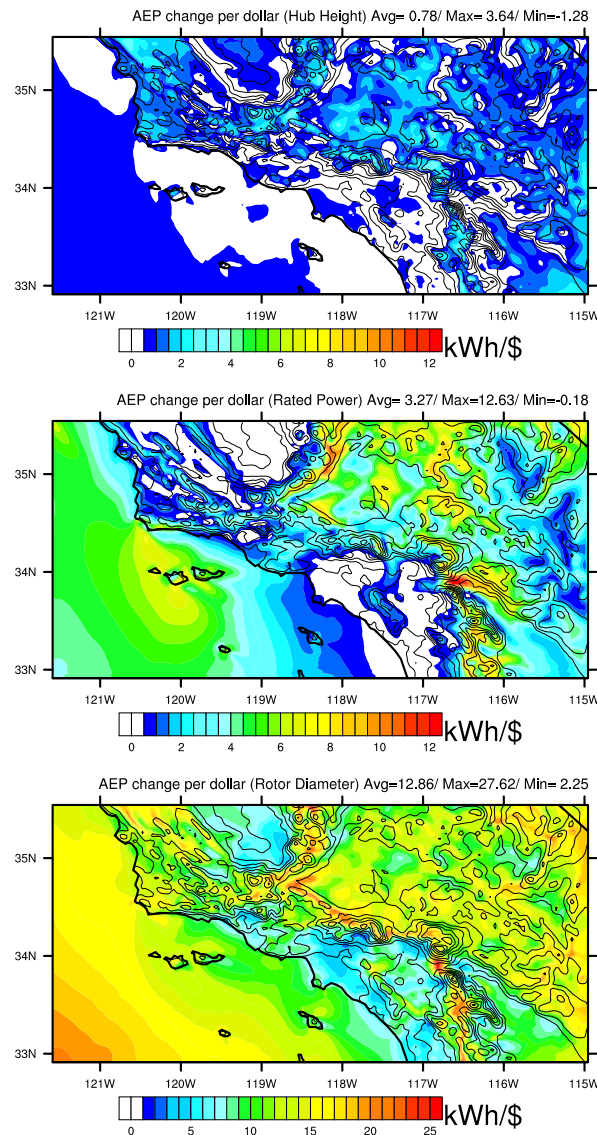


**Figure 10.** AEP change per dollar cost for hub height increments (top panel), rated power (middle panel) and rotor diameter (bottom panel, note: different contour scale). For hub height, the difference in AEP between 120 and 80 m heights divided by the height difference is multiplied by the inverted unit initial capital cost. For rated power (rotor diameter), the difference in AEP between 2.0 and 1.6 MW (100 and 82.5 m) generator power (rotor diameter) divided by the 400 kW (17.5 m) difference is multiplied by the inverted unit capital cost.

of these locations is somewhat offset due to wind speed frequency shifts to faster, more power-generative winds within the lower portions of the distribution. Thus, only some of these locations experience a decrease in energy while most are simply relatively insensitive (below the regression line) to the increase in hub height. Also, shifts in wind speed frequencies within the range between rated and cut-out speeds result in no power gain. Orange markers in the bottom panel of figure 9 denote locations where the wind speed distribution remained almost wholly within this range. Even if there is high shear at such locations, a power gain will not result for an increase in hub height.

## 7. WIND ENERGY CHANGE PER DOLLAR COST

To make an economic comparison between the energy gain resulting from changes to rotor diameter, rated power and hub height, we calculate the change in AEP per unit cost for each characteristic. Out of the three wind turbine characteristics, rotor diameter generally returns the greatest energy per dollar incremental cost for most southern California areas (Figure 10), followed by rated power and, lastly, hub height. On average, the energy change per unit dollar cost is nearly three times higher for rotor diameter increases than for rated power increases, and is more than six times higher than hub height increases. Regions where rotor diameter changes provide the most AEP per dollar incremental cost (greater than  $16 \text{ kWh dollar}^{-1}$ ) include the Tehachapi Mountains, western Mojave, lower elevation zone between the San Gabriel and San Emigdio mountains and San Geronio Pass. Increasing rotor diameter provides upwards of  $10 \text{ kWh dollar}^{-1}$  more compared to rated power for most high desert regions and coastal mountains to the west of the southern San Joaquin Valley. This result is somewhat counter-intuitive in light of the larger number of turbine components that scale with rotor diameter, and may partly reflect the fact that so many southern California locations have a significant fraction of their wind speed distributions between the cut-in and rated speeds, where power generation is quite sensitive to rotor diameter changes.

There are some conspicuous exceptions to the general rule of thumb that investments in rotor diameter provide a greater return in southern California. Regions where AEP is equally sensitive to rotor diameter and rated power changes include the eastern Tehachapi and some Mojave Desert mountains. Areas where AEP gain per dollar cost of rated power increments is greater than that of rotor diameter include the lower desert slopes of the Tehachapi Mountains, the eastern side of the San Geronio Pass and desert slopes of the San Jacinto Mountains and mountains northeast of San Diego (Figure 11). Fast winds at these locations during the onshore wind regime ([23]) which is frequent and prevalent during winter and summer months, respectively, result in the bulk of the wind distribution between the rated and cut-out speeds (Figure 8, middle plot). In regions where the return from investment in more rated power is competitive with rotor diameter, other factors not accounted for in this study may tilt the decision in favor of rated power. For instance, larger rotor radii could create a more pronounced deep array wake effect, motivating the placement of fewer turbines per wind farm area, leading in turn to a reduction in wind farm energy produced [36]. The impact of these wake effect changes cannot be resolved by a mesoscale model.

Wind energy gain per dollar cost is more comparable between rated power and hub height increments (Figure 10, top and middle panels). Rated power increases provide more AEP per dollar cost (exceeding  $4 \text{ kWh dollar}^{-1}$ ) compared to hub height for offshore waters near the Channel Islands, the San Geronio Pass, eastern Tehachapi Mountains and the desert-facing low elevation between the San Gabriel and San Emigdio mountains. Most desert regions realize a greater energy per

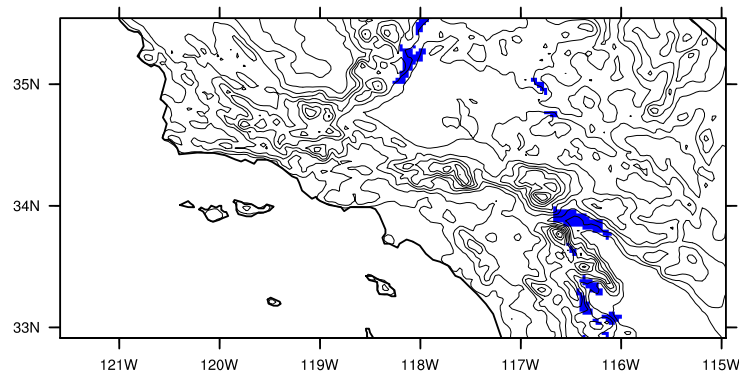


**Figure 11.** Regions where the AEP change per dollar cost for rated power increments exceeds rotor diameter increments.

dollar rated power cost. Limited areas where hub height increments capture more energy per dollar cost compared to rated power include the coastal ranges to the west of the southern San Joaquin Valley, portions of the western Mojave Desert and some high elevations in the San Bernadino Mountains.

With a comparison of WRF winds against only six BLP stations and one SODAR station, we have found WRF's skill to vary depending upon the location and time of day. Given WRF's imperfect performance, we must provide other evidence of the soundness of our study's conclusions insofar as they are based on the realism of the vertical profile of winds. We do this by conducting an observationally-based sensitivity study. In section 7, using figure 10, we concluded that rotor diameter generally returns the greatest AEP per dollar increment cost for most areas of this region of complex topography. We now reconstruct figure 10 by extrapolating vertically the observational timeseries using the power law for three constant atmospheric stability cases intended to span the full range of atmospheric stability states possible in this region (following Wharton and Lundquist, 2010 [20]):

1. Extremely stable:  $\alpha = 0.3$
2. Neutral stability:  $\alpha = 0.1$
3. Extremely unstable:  $\alpha = -0.2$

AEP is calculated for each observed timeseries using the same turbine characteristics and power curves used for our WRF analysis. For both an unstable and neutral assumption, energy gain per dollar invested in rotor diameter is the greatest among the three characteristics for all stations, in agreement with our WRF results (Figure 12(a), unstable not shown). Assuming an extremely stable boundary layer ( $\alpha = 0.3$ ), AEP gain per dollar invested in hub height only exceeds that of rated power for coastal and valley stations, also consistent with our previous findings. Energy gain per dollar invested in rotor diameter exceeds both rated power and hub height for all stations (Figure 12(b)). Only for  $\alpha > 0.3$  do we find results (not shown) that begin to conflict with our WRF analysis in desert and mountain locations. Thus, for our findings

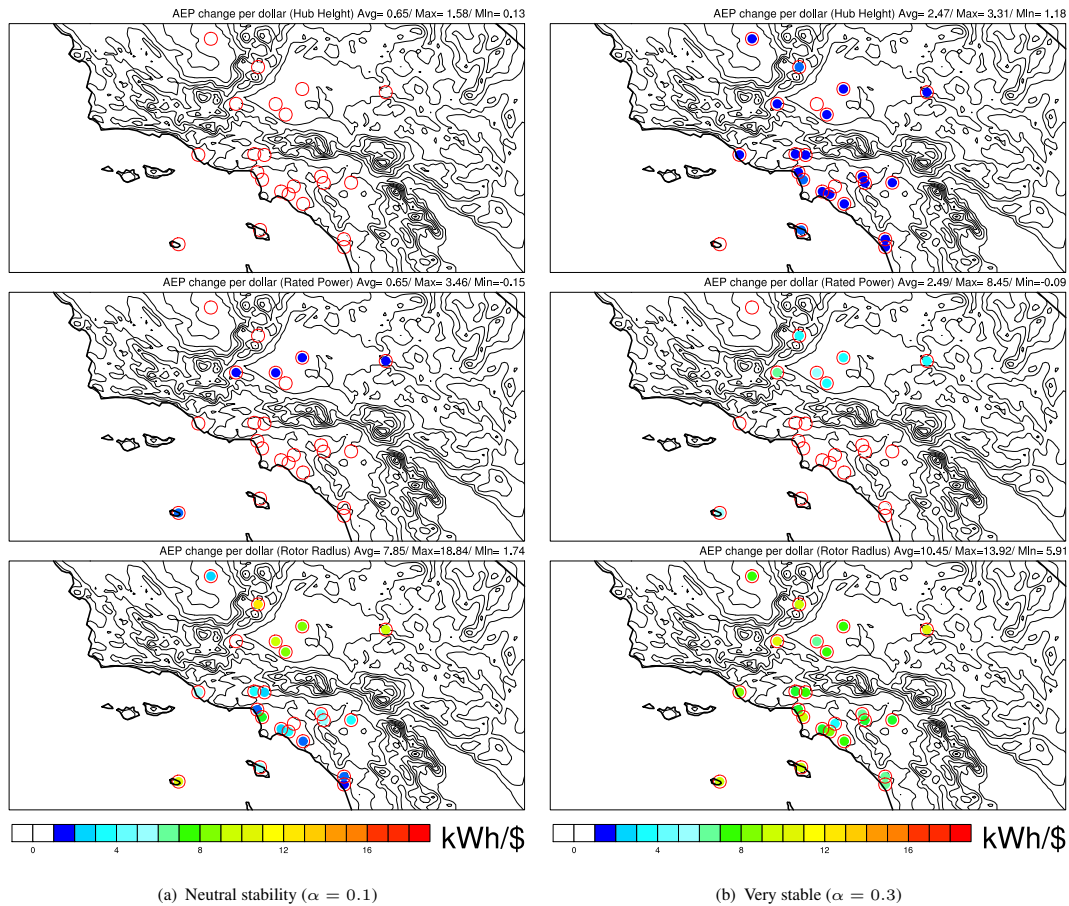


**Figure 12.** Same as figure 10 but for point observations extrapolated vertically using the power law.

presented in figure 10 to be disputed, WRF would have to systematically and severely underpredict atmospheric stability. The positive near-surface wind speed bias (Figure 3(a)) could be a result of over-enhanced vertical mixing as alluded to by other studies for various different conditions and WRF configurations ([31, 29, 26]). However, we have found no evidence of a severe or systematic bias in WRF (albeit for only one SODAR station and six BLPs), consistent with Draxl et al., 2010 [27] who reported high quality WRF vertical wind profile performance for the boundary layer scheme used here (TKE-based MYNN). Therefore, we deem it highly unlikely that the main conclusions based on the WRF output are incorrect.

## 8. CONCLUSION

This study evaluates the sensitivity of southern California annual wind energy production to variations in key characteristics of current wind turbines. Turbine characteristics important for wind power include rotor diameter, rated power and hub

height. Using a validated, meteorological simulation, we find that for each characteristic, the sensitivity of wind energy production has substantial complex geographical variations across southern California. However, further diagnostics reveal that the sensitivity associated with each characteristic is almost perfectly predicted by a single corresponding climate statistic, greatly simplifying understanding of the relationship between climate and turbine optimization for energy production. First, wind energy sensitivity to rotor diameter is directly proportional to the weighted average wind speed between cut-in and rated speed. Second, sensitivity to rated power variations is captured by the percent of the wind speed distribution between the rated and cut-out speeds. Both rotor diameter and rated power sensitivity have a nearly-linear relationship to their corresponding climate statistics. Third, wind energy generation sensitivity to hub height is proportional to lower atmospheric wind shear. Compared to rotor diameter and rated power sensitivities, hub height is least correlated with its climate statistic, though the correlation is still quite high. The strong correlations between wind energy sensitivity and wind speed statistics allow for the estimation of wind energy sensitivity to each of the three turbine characteristics without cumbersome power curve calculations.

To make an economic comparison between the energy gain resulting from changes to rotor diameter, rated power and hub height, we calculate the change in energy per unit cost for each characteristic. Each total incremental cost includes the various turbine component costs that scale with rotor diameter, rated power and hub height changes. We find that rotor diameter increases typically provide a much larger wind energy boost per dollar invested, followed by rated power and hub height. Regions where investment in rated power is competitive or more beneficial include the desert slopes of the Tehachapi Mountains, portions of the Mojave Desert, the eastern side of the San Geronio Pass and the desert slopes of the San Jacinto Mountains and mountains northeast of San Diego. Wind energy gain per dollar cost is more comparable between rated power and hub height increments, with hub height increases resulting in more energy per unit cost for desert regions.

Through joint analysis of regional climate, turbine engineering, and economic modeling, we estimated the energy gain per unit cost resulting from changes to rotor diameter, rated power and hub height without the need for power curve calculations. Because the complex topography of southern California provides a diversity of wind speed distributions, we were able to establish very robust correlations of wind energy sensitivities to climate statistics. It is therefore very likely these results can be applied elsewhere. Thus, using only simple climate statistics (either from a model or meteorological tower), wind farm developers can compare the wind energy gains associated with changes in the three key turbine characteristics. Armed with this information, turbine characteristic costs can then be adjusted to include new costs such as transportation and offshore costs, and arrive at a complete cost/benefit analysis.

For this study, we assess wind energy sensitivity to rotor diameter, rated power and hub height increments. However, rotor diameter and rated power options within the marketplace will continue to evolve over the coming years, changing power curves and wind energy sensitivities. Rotor blade design, generator technology and tower structure innovations will continue to increase rotor efficiency, rated power and hub height, respectively. Thus, a future assessment of wind energy sensitivity to turbine characteristics using updated power curves will be warranted. Still, we anticipate that the general conclusions will remain unchanged, particularly those relating climate statistics to wind energy sensitivity. Further, we acknowledge that the power curves used here are representative of average power output for generic turbines. Actual power curves may differ depending upon the type of turbine and specifics of the environment in which it is embedded, such as the spatial relationship to other turbines and their wakes.

## ACKNOWLEDGEMENTS

The authors are grateful to Kevin Standish for providing invaluable guidance and input regarding turbine power curves and costs. Funding for this study was provided by the U.S. Department of Energy and the City of Los Angeles. SODAR data was provided by the South Coast Air Quality Management District. BLP data was obtained from the Meteorological Assimilation Data Ingest System (MADIS, <http://madis.noaa.gov/>). Surface observations were provided by the National Climatic Data Center.

## REFERENCES

1. Wiser R, Bolinger M. 2010 Wind Technologies Market Report. *U.S. Department of Energy Energy Efficiency & Renewable Energy, DOE/GO-102011-3322* 2011; .
2. Wiser R, Bolinger M. 2011 Wind Technologies Market Report. *U.S. Department of Energy Energy Efficiency & Renewable Energy, LBNL-5559E* 2012; .
3. AWEA. U.S. Wind Industry Year-End 2010 Market Report. *American Wind Energy Association* 2011; .
4. Wiser R, Lantz E, Bolinger M, Hand M. Recent Developments in the Levelized Cost of Energy from U.S. Wind Power Projects 2012; URL <http://eetd.lbl.gov/ea/ems/reports/wind-energy-costs-2-2012.pdf>.
5. Jangamshetti SH, Rau VG. Optimum Siting of Wind Turbine Generators. *IEEE Trans. Energy Convers.* 2001; **16**(1):8–13.

6. Jangamshetti SH, Rau VG. Normalized Power Curves as a Tool for Identification of Optimum Wind Turbine Generator Parameters. *IEEE Trans. Energy Convers.* 2001; **16**(3):283–288.
7. Jowder FA. Wind Power Analysis and Site Matching of Wind Turbine Generators in Kingdom of Bahrain. *Applied Energy* 2009; **86**:538–545.
8. Wiser R, Bolinger M. 2009 Wind Technologies Market Report. *U.S. Department of Energy Energy Efficiency & Renewable Energy, DOE/GO-102010-3107* 2010; .
9. Fingersh L, Hand M, Laxson A. Wind Turbine Design Cost and Scaling Model. *Technical Report NREL/TP-500-40566* 2006; .
10. Skamarock WC, Klemp JB, Dudhia J, Gill DO, Barker DM, Wang W, Powers JG. A Description of the Advanced Research WRF Version 3. *NCAR/TN 475+STR* 2008; .
11. Nakanishi M, Niino H. An Improved Mellor-Yamada Level-3 Model with Condensation Physics: Its Design and Verification. *Bound. Layer Meteor.* 2004; **112**:1–31.
12. Kain JS. The Kain-Fritsch Convective Parameterization: An Update. *J. Appl. Meteor.* 2004; **43**:170–181.
13. Dudhia J. Numerical Study of Convection Observed During the Winter Monsoon Experiment Using a Mesoscale Two-dimensional Model. *J. Atmos. Sci.* 1989; **46**:3077–3107.
14. Mlawer EJ, Taubman PD, Iacono MJ, Clough SA. Radiative Transfer for Inhomogeneous Atmosphere: RRTM, A Validated Correlated-k Model for the Longwave. *J. Geophys. Res.* 1997; **102(D14)**:16 663–16 682.
15. Chen F, Kusaka H, Bornstein R, Ching J, Grimmond CSB, Grossman-Clarke S, Loridan T, Manning KW, Martilli A, Miao S, *et al.*. The Integrated WRF/Urban Modelling System: Development, Evaluation, and Applications to Urban Environmental Problems. *Int. J. Climatol.* 2011; **31**:273–288, doi:10.1002/joc.2158.
16. Chen F, Tewari M, Kusaka H, Warner TT. Current Status of Urban Modeling in the Community Weather Research and Forecast (WRF) Model. *Joint with Sixth Symposium on the Urban Environment and AMS Forum: Managing Our Physical and Natural Resources: Successes and Challenges, Atlanta, GA, USA* 2006; **Amer. Meteor. Soc., CD-ROM. J1.4.**
17. Lo JCF, Yang ZL, Sr RAP. Assessment of Three Dynamical Climate Downscaling Methods using the Weather Research and Forecasting (WRF) Model. *J. Geophys. Res.* 2008; **113(D09112)**, doi:10.1029/2007JD009216.
18. Betz A. Das Maximum der Theoretisch Möglichen Ausnützung des Windes durch Windmotoren. *Zeitschrift für das gesamte Turbinenwesen* 1920; **26**:307–309.

19. Wagner R, Antoniou I, Pedersen SM, Courtney MS, Jorgensen HE. The Influence of the Wind Speed Profile on Wind Turbine Performance Measurements. *Wind Energy* 2009; **12**:348–362, doi:10.1002/we.297.
20. Wharton S, Lundquist JK. Assessing Atmospheric Stability and its Impacts on Rotor-disk Wind Characteristics at an Onshore Wind Farm. *Wind Energ.*. 2011; doi:10.1002/we.483.
21. de Vries O. Fluid Dynamic Aspects of Wind Energy Conversion. *AGARD-AG-243* 1978; .
22. Dvorak MJ, Archer CL, Jacobson MZ. California Offshore Wind Energy Potential. *Renewable Energy* 2010; **35**:1244–1254, doi:10.1016/j.renene.2009.11.022.
23. Conil S, Hall A. Local Regimes of Atmospheric Variability: A Case Study of Southern California. *Journal of Climate* 2006; **19**:4308–4325.
24. Hughes M, Hall A, Fovell R. Dynamical Controls on the Diurnal Cycle of Temperature in Complex Topography. *Climate Dynamics* 2007; **29**:277–292, doi:10.1007/s00382-007-0239-8.
25. Hughes M, Hall A. Local and Synoptic Mechanisms Causing Southern California’s Santa Ana Winds. *Clim. Dyn.* 2010; **34**:847–857, doi:10.1007/s00382-009-0650-4.
26. Storm B, Dudhia J, Basu S, Swift A, Giammanco I. Evaluation of the Weather Research and Forecasting Model on Forecasting Low-level Jets: Implications for Wind Energy. *Wind Energy* 2009; (12):81–90, doi:10.1002/we.288.
27. Draxl C, Hahmann AN, Pena A, Nissen JN, Giebel G. Validation of Boundary-layer Winds from WRF Mesoscale Forecasts with Applications to Wind Energy Forecasting. *19th Symposium on Boundary Layers and Turbulence* 2010; (Paper 1B.1).
28. Chin HNS, Glascoe L, Lundquist J, Wharton S. Impact of WRF Physics and Grid Resolution on Low-level Wind Prediction: Towards the Assessment of Climate Change Impact on Future Wind Power. *Lawrence Livermore National Laboratory (LLNL), LLNL-PROC-425038* 2010; .
29. Shimada S, Ohsawa T, Chikaoka S, Kozai K. Accuracy of the Wind Speed Profile in the Lower PBL as Simulated by the WRF Model. *SOLA* 2011; **7**:109–112, doi:10.2151/sola.2011-028.
30. Clifford KT. WRF-Model Performance for Wind Power Forecasting in the Coast Ranges of Central California. *Master’s Theses, Paper 4043* 2011; .
31. Shimada S, Ohsawa T. Accuracy and Characteristics of Offshore Wind Speeds Simulated by WRF. *SOLA* 2011; **7**:21–24, doi:10.2151/sola.2011-006.
32. Antoniou I, Jorgensen HE, Ormel F, Bradley S, von Hunerbein S, Emeis S, Warmbier G. On the Theory of SODAR Measurement Techniques. *Ris-R-1410(EN)* 2003; .

33. Manwell J, McGowan J, Rogers A. *Wind Energy Explained: Theory, Design and Application*. Second edn., John Wiley & Sons Ltd.: West Sussex, UK, 2009.
34. DOE, NREL. California Wind Map and Resource Potential 2010. URL <http://www.windpoweringamerica.gov/>.
35. Raphael MN. The Santa Ana Winds of California. *Earth Interactions* 2003; **7**(8):1–7.
36. Barthelmie RJ, Jensen LE. Evaluation of Wind Farm Efficiency and Wind Turbine Wakes at the Nysted Offshore Wind Farm. *Wind Energ.* 2010; **13**:573–586, doi:10.1002/we.408.